

Soft Robots for Cluttered Environments Based on Origami Anisotropic Stiffness Structure (OASS) Inspired by Desert Iguana

Renjie Zhu, Dongliang Fan, Wenyu Wu, Chongshan He, Guojie Xu, Jian S. Dai,* and Hongqiang Wang*

Rigidity and softness are essential for robot motion and manipulation in various complex scenarios. To integrate these two contrary features, several variable-stiffness structures are investigated while requiring a longer processing time and more energy for switching from a stiffer to softer status, with only one status at a specific point in time. Inspired by the combined softness–rigidity hybrid property of desert iguanas' skin, the concept of an anisotropic stiffness structure is developed, which simultaneously possesses rigidity and softness properties in different directions, leading to the development of novel soft robots. This anisotropic stiffness structure comprises a silicone–paper composite with multiple superimposed origami patterns and has high stiffness and softness properties. The anisotropic stiffness structure is then constructed by developing three novel soft robots: a crawling robot capable of extending and contracting with a payload of 117 times its own weight, a multifunctional prosthetic hand capable of grasping fragile items with its soft side and lifting and crushing items with its hard side, and a snake robot capable of traveling with the soft side and extruding out with over 75% of its body length with the stiffer side.

manipulation,^[5,6] and search and rescue.^[7] Instead of only having one state (soft or rigid) in a robot, many scenarios necessitate both soft and rigid properties. For example, when picking an item of varying softness, shape, and weight using various motions, such as grasping and fiddling, a packaging robot should be rigid enough to grasp heavy items but soft enough to grasp fragile or irregular items while also being capable of quickly switching between these two states.^[2,8,9] While exploring dangerous and confined environments (e.g., post-earthquake rescue and industrial pipeline inspection), the robot should be sufficiently compliant to adapt to the cluttered environment and rigid to transport a large gap.^[10,11] Moreover, if a robot approaches a rugged surface with a heavy payload, it should be sufficiently compliant to move on the surface and rigid to support the payload.^[12,13]


1. Introduction

Compared to many rigid robots, emerging soft robots possess higher adaptability and safety owing to their compliance,^[1,2] making them a promising solution for human–robot interaction,^[3,4]

To circumvent this problem, researchers attempted to integrate rigid and soft robots. One approach is to convert a robot from a rigid to a soft state and vice versa, which requires a variable-stiffness mechanism. This mechanism has been widely used in wearable robots,^[14] manipulators,^[7,15] and continuum

R. Zhu, C. He, G. Xu, H. Wang
Shenzhen Key Laboratory of Biomimetic Robotics and Intelligent Systems
Department of Mechanical and Energy Engineering
Southern University of Science and Technology
Shenzhen, Guangdong 518055, China
E-mail: wanghq6@sustech.edu.cn

R. Zhu, D. Fan, G. Xu, H. Wang
Guangdong Provincial Key Laboratory of Human-Augmentation and Rehabilitation Robotics in Universities
Southern University of Science and Technology
Shenzhen, Guangdong 518055, China

 The ORCID identification number(s) for the author(s) of this article can be found under <https://doi.org/10.1002/aisy.202200301>.

© 2023 The Authors. Advanced Intelligent Systems published by Wiley-VCH GmbH. This is an open access article under the terms of the Creative Commons Attribution License, which permits use, distribution and reproduction in any medium, provided the original work is properly cited.

DOI: 10.1002/aisy.202200301

R. Zhu, J. S. Dai, H. Wang
Institute of Robotics
Southern University of Science and Technology
Shenzhen, Guangdong 518055, China
E-mail: daijs@sustech.edu.cn

W. Wu
School of System Design and Intelligent Manufacturing
Southern University of Science and Technology
Shenzhen, Guangdong 518055, China

J. S. Dai
Centre for Robotics Research
Department of Engineering
King's College London, Strand
London WC2R 2LS, UK

H. Wang
Southern Marine Science and Engineering Guangdong Laboratory (Guangzhou)
Guangzhou, Guangdong 511458, China

robots,^[16,17] relying on functional materials (e.g., thermally sensitive materials,^[18–20] and dielectric elastomer actuators,^[21,22] magnetorheological [MR], and electrorheological [ER] fluids^[23,24]). However, the stiffness state transition typically requires external stimuli (e.g., external electric or magnetic fields for ER or MR), complex structures, or a large power supply.^[22] This typically takes more time (e.g., a shape-memory polymer needs more than 30 s for heating and 4 min for cooling^[19]). In addition, a variable-stiffness robot can only stay in either the soft or rigid state, but cannot retain both properties in one structure simultaneously.

Desert iguana (*Dipsosaurus dorsalis*) encounters similar survival challenges in its harsh natural environment. Its skin is sufficiently rigid to protect soft organs from hard and heavy objects (e.g., flying stones^[25–27]). The skin should also be sufficiently compliant for extension and compression, allowing the body to navigate agilely within a complex cave.^[28,29] With the evolution of millions of years, desert iguanas' skin has excellent properties of being rigid and compliant simultaneously along different directions with pyramid-shaped hard scales made of the β -keratins and flexible tissue (α -keratins^[28,30,31]).

Many materials^[32,33] and manufacturing methods^[32,34,35] are available to implement this specific mechanism. However, as a type of metamaterial, the origami structure is a distinguished approach owing to its low cost, lightweight, and simple manufacturing.^[36,37] Owing to their various benefits, origami structures have demonstrated great potential for applications in a variety of scenarios, for example, reconfigurable structures,^[38–40] biomedical robots,^[41,42] soft grippers,^[43–46] and crawling robots.^[39,47,48] Among various origami structures, the pyramid-shaped bulges in the Miura-ori structure are similar to iguanas' scales.^[49–54] Researchers have observed that, by combining two open Miura-ori patterns into a closed origami tube, the geometric topology achieved by folding, rather than the base material, exhibited unique mechanical properties.^[49,54–59] Unfortunately, most previous studies have concentrated on the geometries and fundamental mechanics of the structure, with few applications to robots.

In this article, inspired by the Miura-ori structure, we propose a novel design of the origami anisotropic stiffness structure (OASS) to solve the problem of both soft and rigid states demanded in one structure and promote the versatility of robots (Figure 1A). In contrast to variable-stiffness structures that require longer time and specific stimuli to achieve soft–rigid status switching, the OASS combines both rigid and soft properties along different directions in a single structure, with both soft and rigid states coexisting. In this study, we designed the OASS module using an origami-inspired structure (similar to desert iguana's pyramid-shaped hard scales) with anisotropic stiffness. The anisotropic stiffness structure was made with a paper and silicone composite (similar to the composite materials of the desert iguana skin) for greater resilience and robustness of the robots under dynamic and repetitive damage forces (Figure 1B). We fabricated different OASS actuators and robots by arranging modules with different shapes and sizes. In the prototypes, the stiffness ratios for bending and compression of the OASS actuator were as high as 38.5 and 37.9, respectively. The significant impact of the OASS can be observed in our construction of the following three soft robots based on the OASS. They

are a 1) crawling robot that was soft enough to shrink and expand to move forward but also rigid enough in the vertical direction to carry a payload 117 times heavier than its weight; 2) prosthetic hand that was sufficiently compliant to fragile or irregular items but also rigid enough in the lateral direction to even smash an egg by a knife-hand strike; and 3) snake-shaped robot made by connecting multiple OASS actuators traveled by the body waves generated by the bending of the actuators (using the soft side) and surpassed a gap larger than 75% of the body length owing to the high stiffness of the rigid side.

2. Results and Discussion

2.1. Design of the OASS (Origami Anisotropic Stiffness Structure)

Desert iguanas' skin, which possesses many pyramid-shaped hard scales^[25–27,30] (Figure 1B), is rigid to protect the iguanas from the strong attack of flying stones and sands and compliant to allow freedom of body movement.^[29,31] We replicated this property using origami-inspired structures, which can achieve unique mechanical features owing to the limitations of the composed materials (Figure 1B). Here, we selected this structure that comprises arrays of pyramid-shaped bulges,^[25,27,30] similar to the topology of the iguanas' skin (Figure 1B). This structure can endure strong forces in one direction, but is susceptible to compression or bending in another direction. We can generate robots of various shapes and functions for various applications by arranging the OASS molecule tubes of different lengths into various topologies (Figure 2A).

2.2. Parametric Analyses of the OASS

Here, we analyzed the anisotropic compression and bending stiffnesses on six primary parameters (Figure 2A,B). Here, l represents the length of the ridge; θ the angle between the two ridges; t the thickness of the shell; s the cross-sectional area of the OASS molecule tube; and m and n the number of bulges in the y and x directions, respectively. The following analyses are based on the simulation model described in Materials and Methods section.

In this study, we used a 3×4 OASS actuator (Figure 2B) that combines multiple OASS molecule tubes as an example for the analysis of compression stiffness (Figure S1A, Supporting Information). The OASS is susceptible to lateral shrinking or expansion when subjected to a weak horizontal force, while it can resist a strong vertical force. This is because the stiffness in the z direction (K_z) is significantly larger than that in the x direction (K_x) or y direction (K_y). Because K_y is comparable to K_x in the magnitude, we only evaluated K_y for conciseness in the following analysis. As shown in Figure 2C, when the size of the OASS scales up (i.e., $m \times n$ increases from 2×2 to 6×8), K_z increases steadily because more bulges participate in load bearing. The stiffness ratio $K(=K_z/K_y)$ approached 41 for a 6×6 actuator. By connecting more bulges in series, K_y was reduced, and the stiffness ratio K increased (Figures 2C, S2B, S2C, S3B, and S3C, Supporting Information). However, if more bulges were connected in parallel, K was slightly reduced

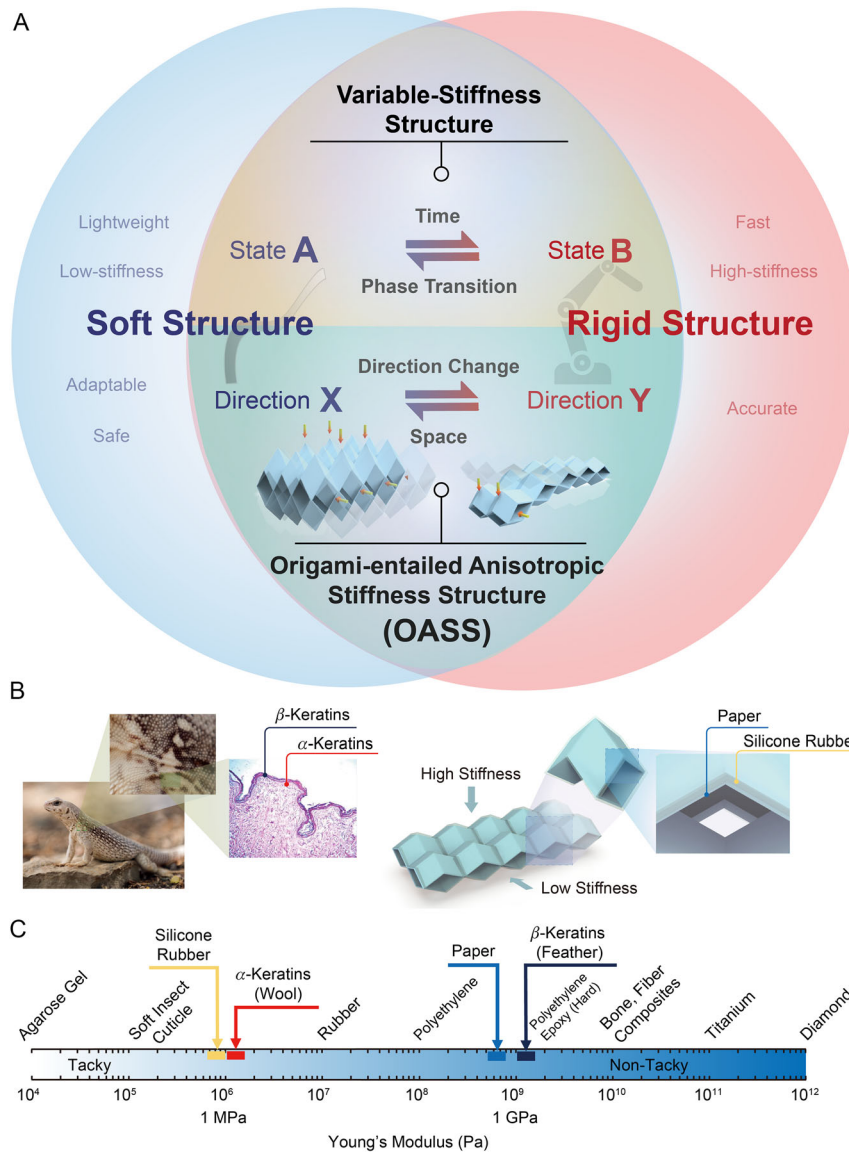


Figure 1. Concept of the origami anisotropic stiffness structure (OASS). A) Comparison of the rigid structures, the soft structures, the variable-stiffness structures, and the OASS. The bioinspired OASS consists of B) a pyramid-shaped array structure and C) a soft–rigid composite material, similar to desert iguanas' scale array structure and skin material, respectively. The images in (B) are adapted with permission from Ref. [30] under 200 \times magnification.

(Figures 2C, S2D, S2E, S3D, and S3E, Supporting Information). Interestingly, the stiffness ratio differed for the same area (i.e., the same number of bulges) if the shapes were not the same. For instance, the stiffness ratio K for the 6×6 actuator was approximately four times higher than that of the 4×9 actuator (Figure S4, Supporting Information). The reason of this phenomenon is because the bulges along the actuator boundary receive less supporting force from other bulges, and hence they are less stiff (Figures S2A, S3A, S4A, and S5, Supporting Information). Its maximum stiffness appeared in the z direction and its minimum in the y direction (Figure 2D). We also compared the effects of different angles θ , length l , and thickness t on stiffness (Figure 2E,F). The stiffness ratios are K and K_z peak (although K_y is minimized) when θ is approximately 60° . In

addition, both K_z and K_y decline when the ridge length l increases because a longer ridge l is more likely to buckle. Compared with the ratio K_z , the ratio K_y drops more drastically, and hence, the stiffness ratio K increases for a longer ridge. Moreover, a thicker t of OASS actuators increases the stiffness in both y and z directions simultaneously (Figure 2F); however, it decreases the stiffness ratio because the increase rate of K_y is higher than that of K_z . This tendency was also true for different ridge lengths. In summary, to achieve a higher stiffness ratio, we can increase the number of bulges and ridge length, reduce the layer thickness, and approximate the ridge angle to 60° .

Similarly, for anisotropic bending stiffness, we can combine the OASS module tubes into a 2×5 actuator (Figures 2G and S1B, Supporting Information). The maximum stiffness appeared

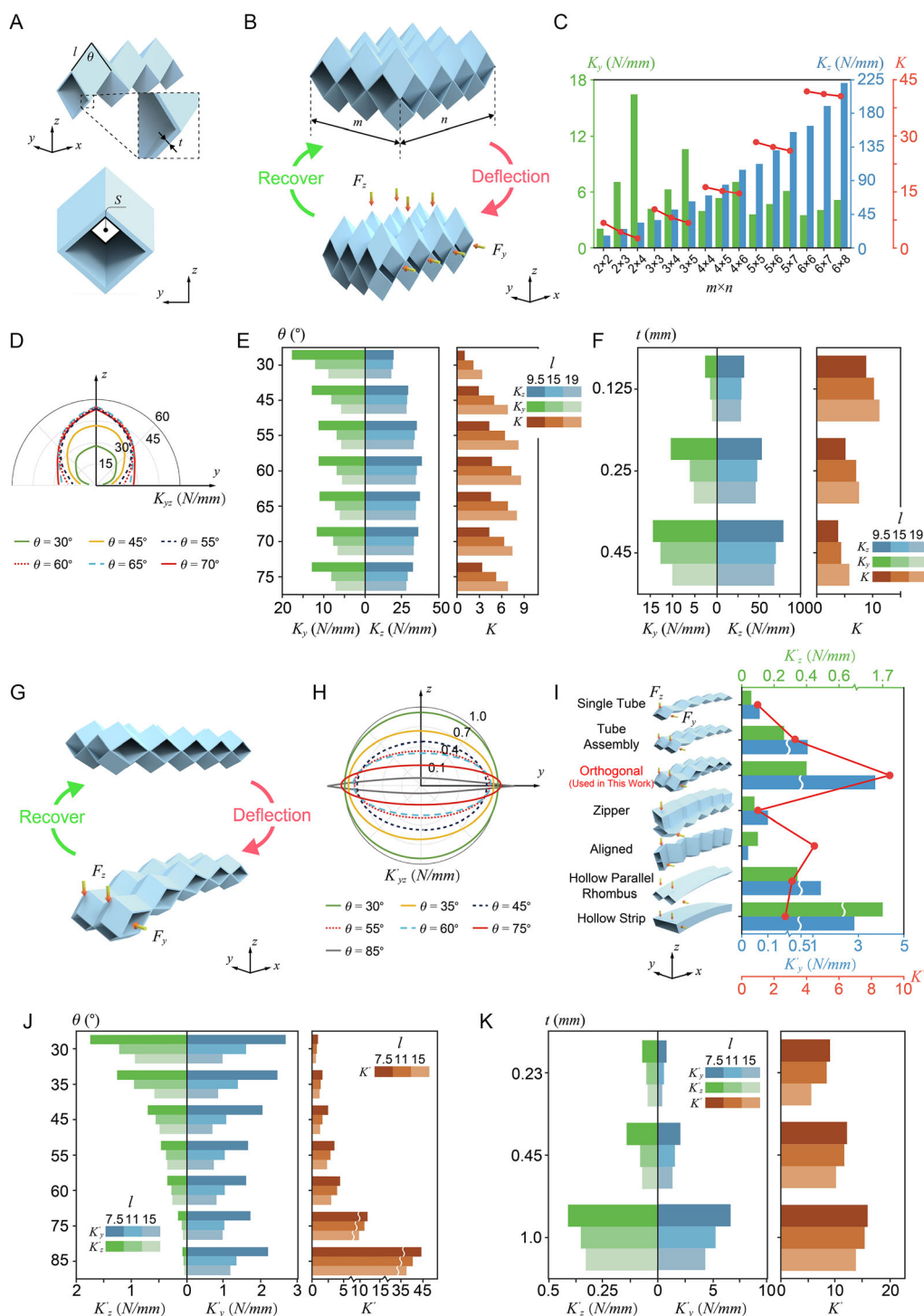


Figure 2. Parametric analysis of the OASS. A) Parameters on an OASS molecule. B) Initial and deformed geometries of the 3×4 OASS actuator when F_y and F_z are applied on it in different directions. C) Compression stiffness K_y and K_z under different values of $m \times n$, l , and t are 60° , 19 mm, and 0.25 mm, respectively. D) Compression stiffness for loads in the y - z plane represented as a radial plot under different ridge angles θ . Stiffness is shown as distance from the origin. l and t are 19 and 0.25 mm, respectively. E, F) Compression stiffness K_y , K_z , and K under various values of θ , l , and t . G) Initial and deformed geometries of the 2×5 OASS actuator when the right end is fixed, and F_y and F_z are applied on the left end in different directions. H) Bending stiffness for loads in the y - z plane represented as a radial plot under different ridge angles θ . Stiffness is shown as distance from the origin. l and t are 15 and 0.45 mm, respectively. I) Bending stiffness K'_y , K'_z , and $K' (=K'_y/K'_z)$ in different structures, where zipper and aligned structures are adapted from Ref. [51]. J, K) Bending stiffness K'_y , K'_z , and K' under various values of θ , l , and t .

in the γ direction and the minimum in the z direction (Figure 2H). In the following analysis, K'_γ and K'_z represent the bending stiffness in the γ and z directions, respectively. Compared with other structures, the OASS actuator possessed the maximum stiffness ratio ($K' = K'_\gamma/K'_z$), nine, which was twice higher than the second one (Figure 2I). In this pattern, typically, larger θ decreases both K'_z and K'_γ , except that, when θ is larger than 60° , θ increases K'_γ . The stiffness ratio K' increased as θ approached 90° (Figure 2J). For instance, the stiffness ratio was only 1.07 when θ was 30° , it became 42 times larger (44.7) when θ was 85° . In addition, K'_γ , K'_z , and K' all increased when the shell thickness t increased or the ridge length l decreased (Figure 2K). Furthermore, when the size of the OASS actuator scaled up (i.e., $m \times n$ increases from 2×2 to 2×10), both K'_γ and K'_z decreased simultaneously, and when n was greater than 4, K' tended to be constant (Figure S6, Supporting Information). In summary, to increase the bending stiffness ratio, we can increase θ and t but reduce l .

Based on the aforementioned parametric analysis of the finite element analysis (FEA) model, we obtained the relationship between the five primary parameters (l , θ , t , m , and n) and anisotropic compression stiffness (K) and anisotropic bending stiffness (K'). Subsequently, we selected a structure with suitable parameters and performed experimental verification.

2.3. Characterization of the OASS

We tested the compression stiffness of the four OASS actuators ($\theta = 60^\circ$, $l = 19$ mm, and $t = 0.25$ mm) in both γ and z directions (Figure 3A). During a single compression test, 6×6 OASS actuator 1 made of polylactic acid (PLA) and actuator 2 made of pure paper (PP) achieved stiffness ratios of 37.9 and 36.7, respectively, consistent with the simulation results (Figure 2C). There is very little discrepancy between the experimental and simulation results owing to the geometrical errors of the actuators from manual manufacturing. The experimental results for 3×4 OASS actuators 3 and 4 are shown in Figure 3A. Although the materials do not influence the stiffness ratio, the structure with the silicone–paper composite (SP) showed higher reliability than those made of PP. As shown in Figures 3B and S7, Supporting Information, the SP expands the elastic region of the actuator by more than twice (e.g., from 6 mm for the PP actuator to more than 10 mm for the SP actuator). The PP OASS actuator suffered irreversible shell deformation (i.e., wrinkles and collapse) after a large compression. Moreover, after 100 compression cycles, the supporting force of the SP actuator degraded by 40 N at the 6 mm displacement, and only 30% of the decreasing value of the counterparts were made of PP (135 N), as shown in Figure 3B. The detailed simulation and experimental methods are provided in Experimental Section.

To test the anisotropic bending stiffness, 2×5 OASS actuators were used as examples. As shown in Figure 3C, with a larger θ , the stiffness ratio (K') increased significantly (11 when $\theta = 75^\circ$ and 38.5 when $\theta = 85^\circ$). As shown in Figure 3D, the OASS actuator with composite shells and the metamaterial structure demonstrated a large difference between the deflections in different directions (larger stiffness ratio), whereas the stiffness of a solid soft structure made of the same geometry is constant.

The aforementioned tendencies regarding the compression/bending stiffness ratio do not vary with the materials, which is proven by the comparison results of models with different θ made of different Young's modulus materials (Figures S7 and S8, Supporting Information). However, the absolute value of stiffness varies with the material. Vast materials can be selected based on the specified scenarios. In practice, this structure with a hollow chamber can barely be made of a soft, thin shell because the soft material cannot support its own weight and is susceptible to collapse. Moreover, the total weight unfavorably increases if the soft shell becomes thicker. If the shell is too thick (in the extreme case, the chamber becomes solid), the structure is no longer a metamaterial (i.e., it has no anisotropic characteristics). Conversely, if the shell of the OASS is made of stiff material, the elastic range is usually small.^[37,60]

Thus, in this study, we used an SP as the primary material for modules and robots. Using the composite material, both the elastic range and resilience of the structure are enhanced (the details are provided in the next section). Moreover, this material is easily achievable, economical, and lightweight.^[36] With this composite, a complex structure of pyramid arrays can be made by the manual fabrication process of a well-studied origami structure.^[36,37,43] Furthermore, this structure could be integrated with electrical circuits, sensors, controllers, etc., for extensive future applications.^[36,37]

2.4. Demonstrative Applications of the OASS-based Soft Robots

Typically, rigid and soft robots are utilized in different scenarios because of their opposite properties: soft robots are adaptable and lightweight, whereas their rigid counterparts are usually stiff and supportive. Robots that integrate OASS actuators are expected to be more versatile and available for most conventional applications that require either soft or rigid robots. The OASS-based robot is adequate for fitting more complex scenarios. For example, some scenarios might require that low stiffness exists in one direction and high stiffness in another (e.g., a soft robot capable of bearing a heavy payload), or that the robot's body should shift between high and low stiffness frequently and efficiently (e.g., dexterous manipulation). Many soft and rigid robots cannot operate in these cases. In this study, we demonstrated the extensive impacts of OASS actuators using a heavy load-bearing crawling robot, dexterous prosthetic hand, and multifunctional snake robot.

2.4.1. Crawling Robot Capable of Carrying an Ultraheavy Payload

In surveillance, exploration, search, and rescue, the capability to carry heavy equipment and supplies is highly desirable. Compared to conventional rigid robots, soft robots can easily navigate in a cluttered environment because of their high compliance.^[10,61,62] However, the payload capacity of some soft robots driven by pneumatic pressure (the most dominant actuation method^[13,63,64]) is usually low because a heavy payload on the back is more likely to squeeze the compliant air path and consequently adversely affect the movement of the robot (Movie S1, Supporting Information). Although it is a smart method to

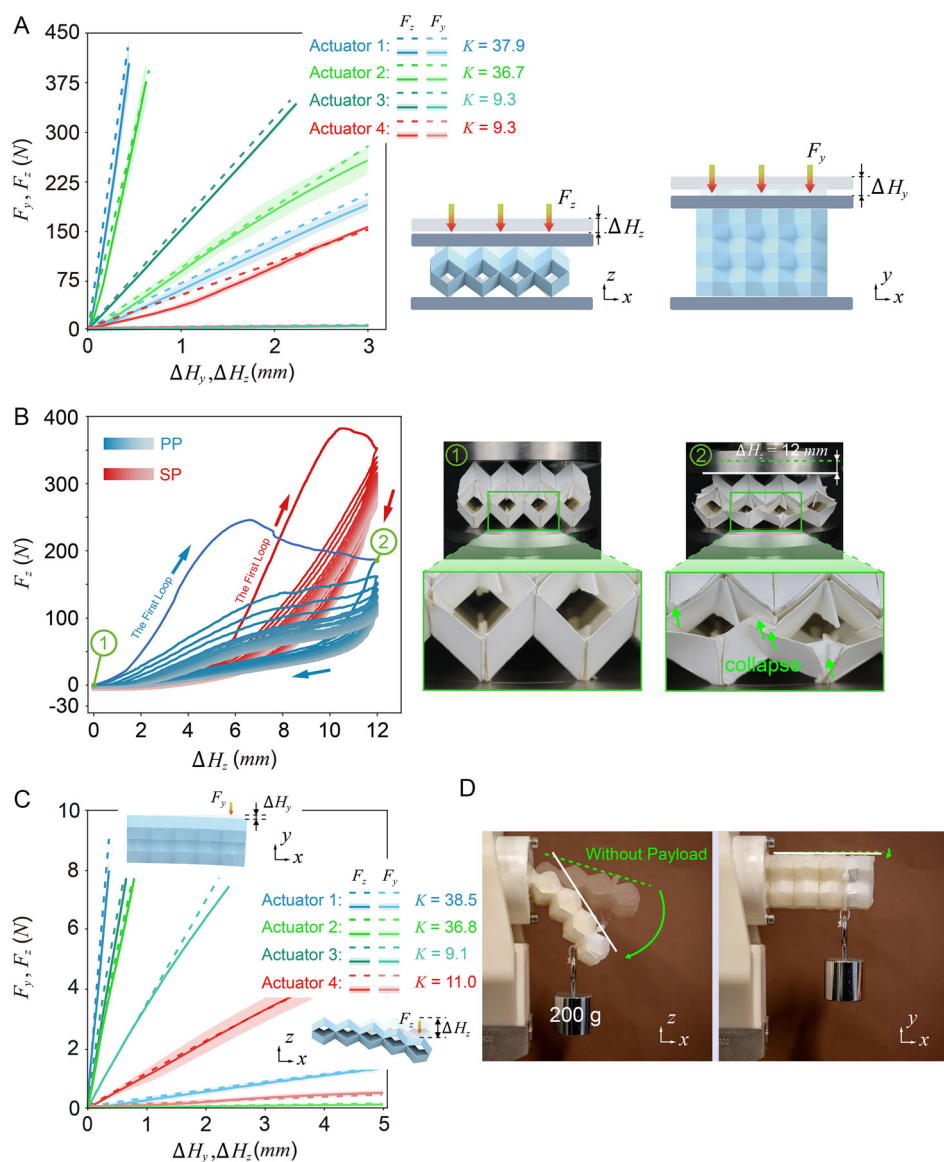


Figure 3. Characterization of the anisotropic stiffness of the OASS. A) The compression force-displacement curvatures of 6×6 OASS actuators 1 and 2 made of polylactic acid (PLA) and pure paper (PP), respectively. Actuators 3 and 4 (3×4 pyramids) are made of PLA and PP, respectively. The solid and dotted lines indicate the experimental and simulation data, respectively. B) The comparison of the force-displacement curvatures of OASS actuators made of PP and silicone–paper composite (SP), tested under 100 compression loops in the z direction. The colors from deep to light indicate the experimental loops from 1 to 100. C) The bending force-displacement curvatures of four 2×5 OASS actuators (actuators 1 and 2 made of PLA and PP, respectively [$\theta = 85^\circ$, $l = 11$ mm, and $t = 0.45$ mm]), and actuators 3 and 4 made of PLA and PP, respectively [$\theta = 75^\circ$, $l = 11$ mm and $t = 0.45$ mm]). The solid and dotted lines indicate the experimental and simulation results, respectively. D) Demonstration of the anisotropic stiffness of an OASS actuator.

unload cargo from the main body back and drag the load, it has great limitations for movement on complex terrains.^[13,65]

We created two OASS-based crawling robots that were soft in the horizontal direction but stiff in the vertical direction to protect the air path from a heavy payload (Figure 4A,B). When the vacuum is turned on and off, the robot shrinks and expands horizontally. Because its driving force is proportional to the cross-sectional area (s) of the air path in the actuator (Figure 2A), the largest shrink driving force is generated when s is the largest (i.e., $\theta = 60^\circ$, Figure S10, Supporting Information).

Furthermore, the small robot of only $30 \times$ g withstood a payload of 8.4 kg, 280 times heavier than its weight (Figure 4A). While moving, it carried a 3.4 kg payload, 117 times its weight (Figure 4C and Movie S1, Supporting Information), and almost 18 times the maximum payload for some existing robots (Refs. [13,22,61,64–70]; Figure 4E). With more OASS module tubes (6×8 OASS actuator; Figure 4B), the robot was capable of carrying a lady volunteer (≈ 46 kg; Figure 4D and Movie S2, Supporting Information) and moved forward on the ground. The advantageous features of the OASS crawling robots, such as compactness, light weight, low cost, adaptation to the

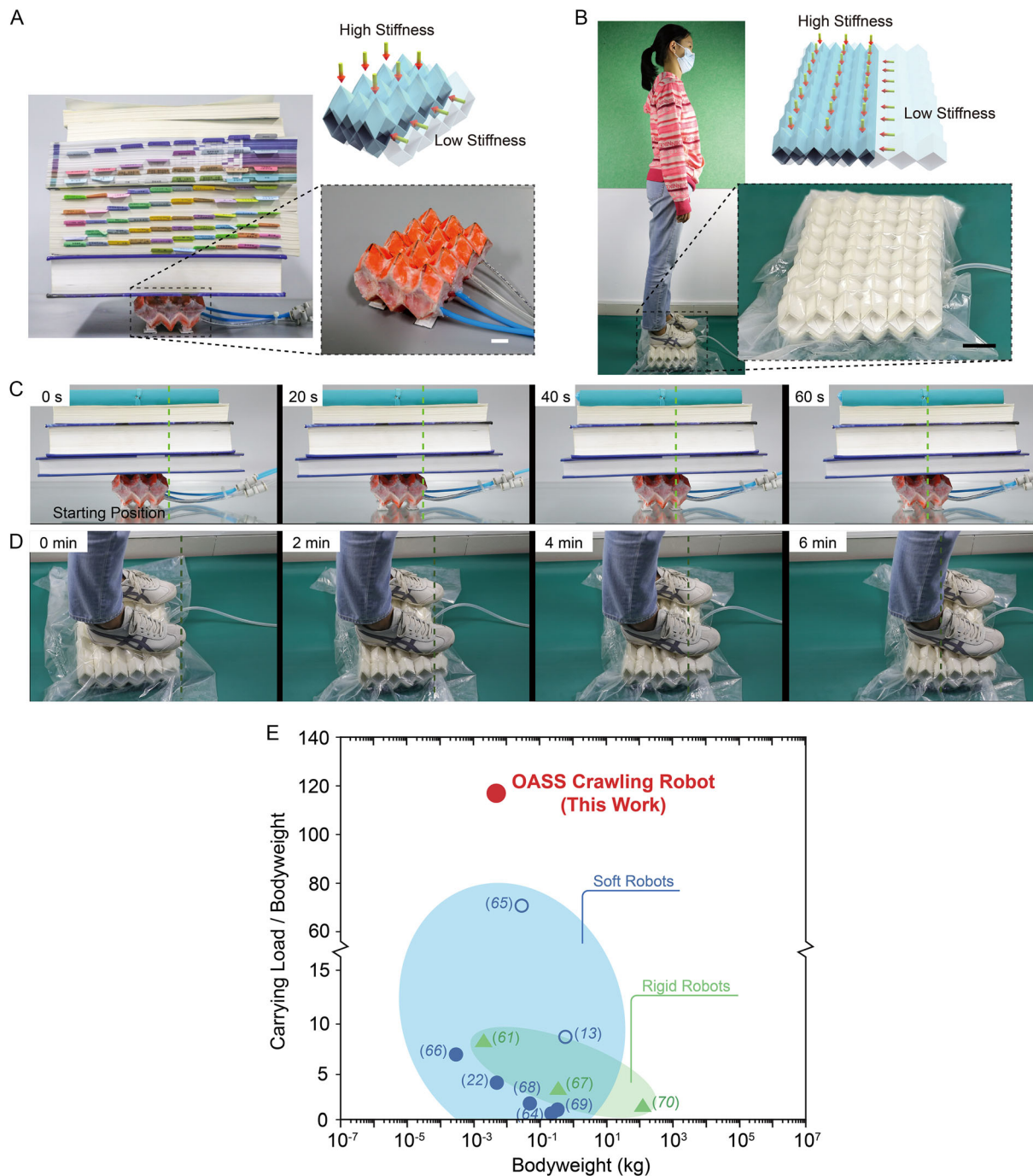


Figure 4. The load-crawling robot made of the OASS. A) The small crawling robot (30 g, $55 \times 115 \times 25$ mm) carrying a 3.5 kg payload. Scale bar is 10 mm. B) The big crawling robot (≈ 1.2 kg, $250 \times 400 \times 100$ mm) carrying a young man (≈ 46 kg). Scale bar is 50 mm. C, D) The snapshots when the small and big crawling robots move forward while carrying a heavy payload, respectively. E) Load capacity versus bodyweight for different kinds of robots. The filled symbols represent the payload carried on the back of the robot, and the empty symbols represent the payload dragged by the robot on the ground.

environment, and high load-carrying capacity, make it a promising solution for heavy goods transportation in a cluttered environment, and are potentially available for applications such as search and rescue on uncluttered terrains and exploration on icy surfaces, where wheeled vehicles hardly move.

2.4.2. Prosthetic Hand

Robotic manipulation is critical for various applications, such as exploration, delivery, packaging, and prosthetics. This is a challenge because the properties of objects, such as size, shape,

and softness, vary broadly. In this study, a prosthetic hand was used as an example. Most previous prosthetic hands consisted of rigid metal components. Thus, they were heavy, rigid, susceptible to impact, and difficult to handle deformable objects (e.g., an egg, banana, or badminton) or fragile objects.^[71,72] Comparably, the emerging soft prosthetics promise to address these problems. However, they can only provide a strong output force or maintain their shape when subjected to an external force in manipulation.^[72,73]

We built an anisotropic stiffness hand using the OASS actuators (Figure 5A), which can quickly switch stiffness (by simply

shifting the working direction), consumes little energy, and is versatile, lightweight (1.8 kg), and low cost (\$263.4; Table S1, Supporting Information). The detailed design and fabrication methods are provided in Materials and Methods. In comparison, we also built a solid–soft hand of the same size and geometry made of silicone rubber and driven by cables. Both the phantom solid–soft hand and the OASS hand (with its soft side) could bend naturally inward to grab irregularly shaped or fragile items (Figure 5B and Movie S3, Supporting Information). However, the solid–soft hand, similar to those in previous reports, failed to grab plate items (Figure 5C and Movie S4,

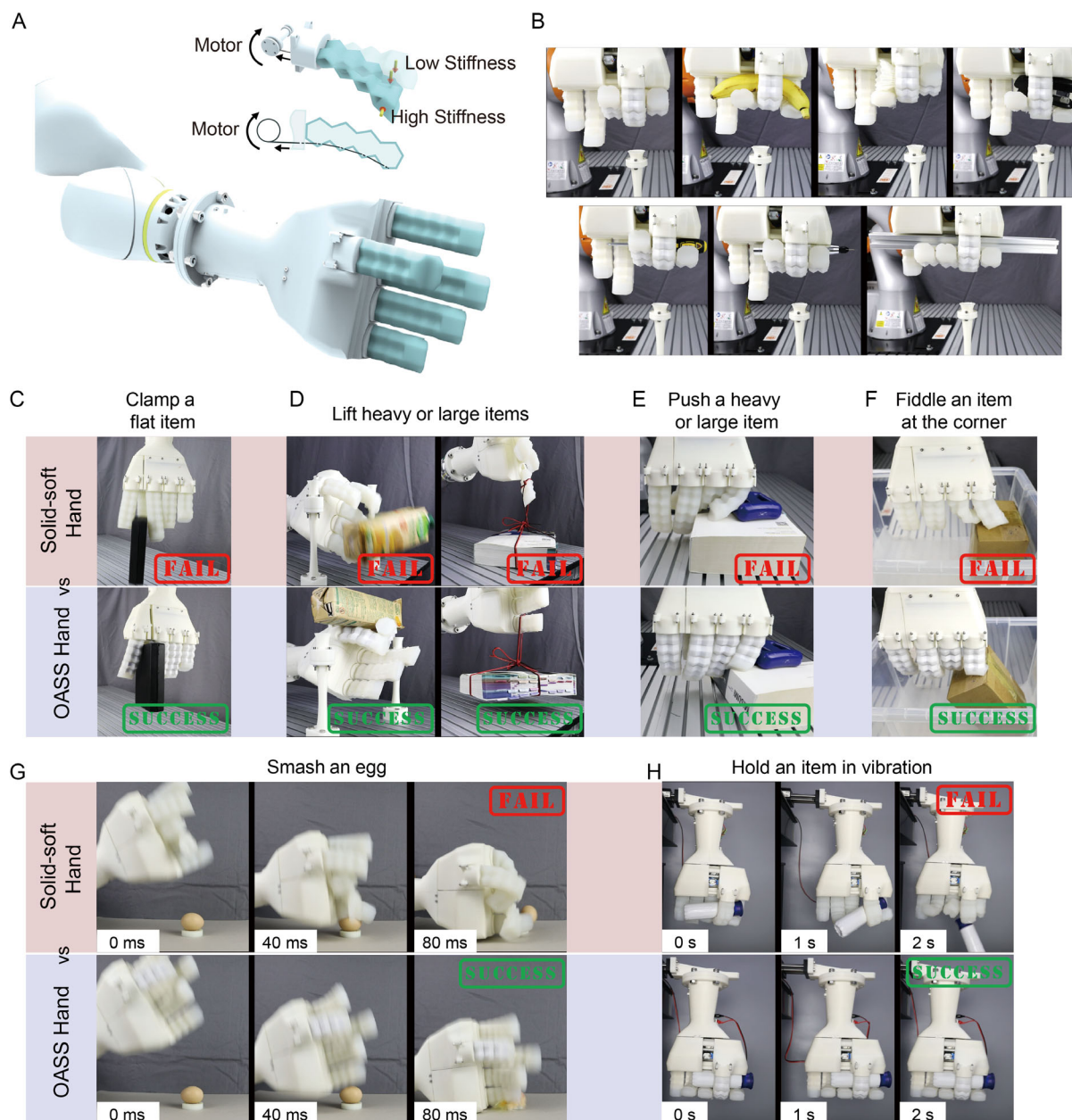


Figure 5. The prosthetic handmade of the OASS. A) The structure and driving mechanism of the OASS prosthetic hand. B) The OASS hand grabbing various irregular shaped or fragile items. Comparison between the solid–soft hand and the OASS hand while C) clamping a flat item, D) lifting up heavy or large items, E) pushing heavy and large items on the ground, F) fiddling an item at the corner of a box, G) smashing an egg, and H) holding an item under a fast horizontal oscillation.

Supporting Information), lift large or heavy items (i.e., 1.5 kg milk box and 1.8 kg book; Figure 5D and Movie S5, Supporting Information), push a bulky item (≈ 2.5 kg) on the plane (Figure 5E and Movie S6, Supporting Information), or fiddle an item at the corner of a box (Figure 5F and Movie S7, Supporting Information) because of poor rigidity. Conversely, the OASS hand completed these tasks by shifting the effective direction to the high-stiffness side. With its rigid side, the OASS hand could even smash an egg (Figure 5G and Movie S8, Supporting Information), such as a knife-hand strike in martial arts.

Moreover, being rigid or soft in different directions is critical for various manipulation tasks. For example, to pick and place fast,^[74,75] the hand should be soft enough to hold an irregular object tightly and rigid enough in the moving direction to transmit high acceleration from the motor to the object. As shown in Figure 5H and Movie S9, Supporting Information, the phantom soft fingers left the initial positions and bent largely because of the high acceleration; consequently, the item slipped out of the phantom hand. Most previous variable-stiffness robotic hands were not adequate for this case, wherein the hands were either too soft or too rigid.^[7,20] Conversely, the OASS hand held the item firmly based on the synergistic work of softness and rigidity,

although the hand moved quickly with 4 m s^{-1} at speed and with 4 m s^{-2} at acceleration (Figure 5H).

2.4.3. Snake-shaped Robot

Snake robots, as promising platforms for post-earthquake rescue and industrial pipeline inspection, can replace humans in restricted and dangerous environments.^[47,76] Traditional snake-shaped robots made of rigid links and servo motors^[77,78] possess limited compliance, whereas recently emerging soft snake robots cannot support their weight to cross large gaps owing to their low stiffness.^[65,76]

We devised a snake-shaped robot by connecting two OASS actuators in series (Figure 6A). It is characterized by both anisotropic compression and bending stiffness and has a high-stiffness side to carry a heavy payload or cross a large gap and a low-stiffness side to create body waves and travel on the ground similar to a snake (Figure 6B). The motion of the robot was enabled by vacuuming and deforming the two OASS actuators sequentially (Figure 6C and Movie S10, Supporting Information). Our tests demonstrated that the robot moved continuously while carrying a 1 kg payload or even being buried by

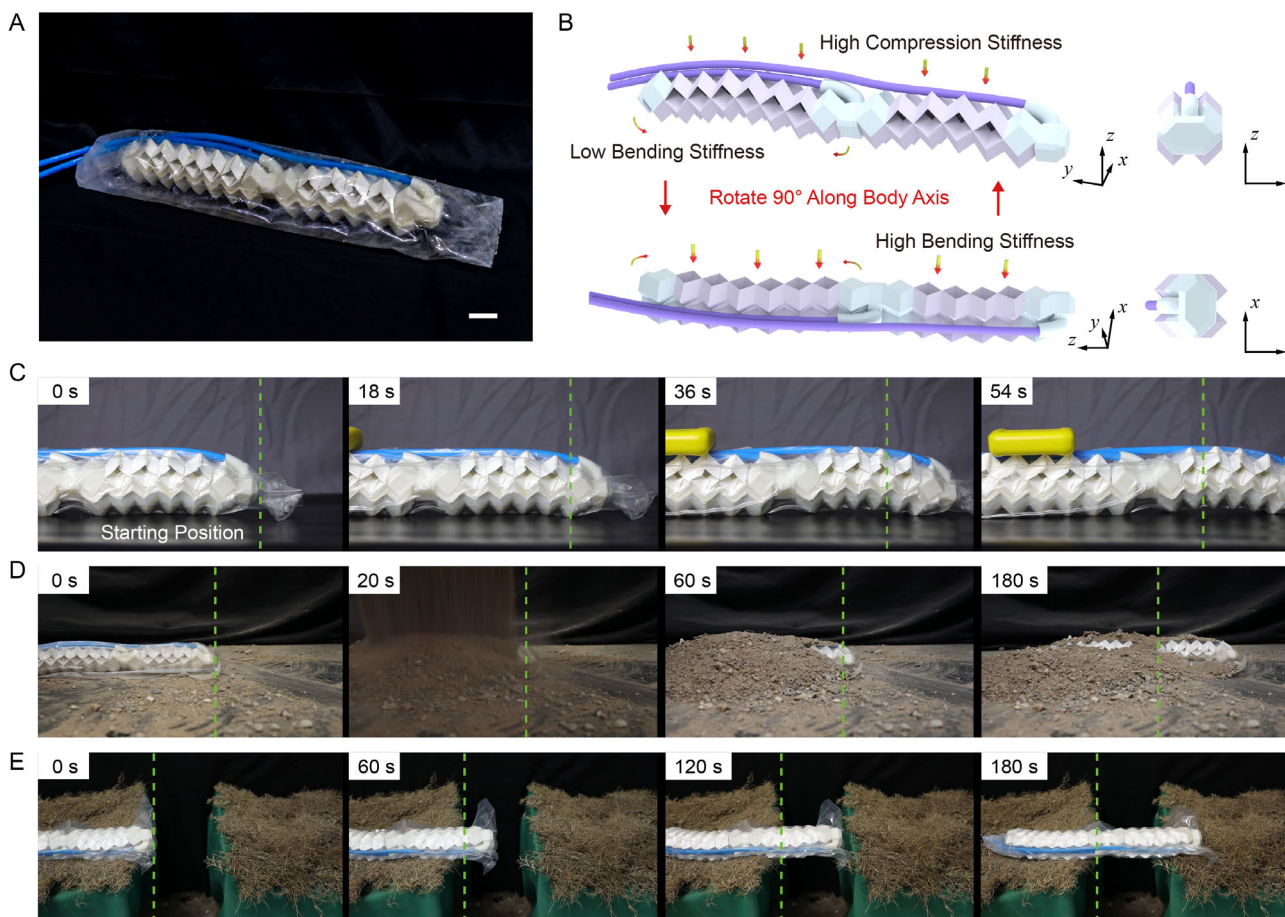


Figure 6. The snake-shaped robot made of the OASS. A) The structure of the snake-shaped robot. Scale bar is 40 mm. B) The anisotropic compression and bending stiffness of the OASS snake-shaped robot. C) The robot moves forward while carrying a 1 kg payload. D) The robot moves after being buried by soils and cabinets. E) The robot crosses a gap by its high stiffness side.

heavy objects (e.g., soils and cabinets), making it promising for post-disaster search and rescue (Figure 6D and Movie S11, Supporting Information). On the rigid side, it spanned air with 50% of its body length to pass a large gap (Figure 6E and Movie S12, Supporting Information). Its stiffness can support a larger extrude length; however, the robot is likely to fall down once the center of gravity is out of the ground. When a heavy payload is located at the end of the force balance, it can stretch out by more than 75% of its body length to reach the target, similar to a real snake (Movie S12, Supporting Information).

3. Conclusions

Inspired by the soft–rigid hybrid characteristics of desert iguanas' skin, we proposed the concept of the OASS. In an OASS, the compression stiffness varies in different directions, as does the bending stiffness. In this study, the influences of the length, ridge angle, thickness, and other parameters on the stiffness ratios were analyzed, and OASS actuators with a compression stiffness ratio as high as 37.9 and a bending stiffness ratio of more than 38.5 were implemented. This study proved the extensive impact of OASS using three novel soft robot prototypes in different scenarios. By integrating the OASS, the crawling robot can bear a payload 117 times heavier than its weight, making it promising for transportation on uncluttered terrains. The second prototype is a versatile OASS prosthetic hand that can gently grasp a fragile and irregular item by the soft side and clamp, lift, fiddle, or even smash an item on the rigid side. This hand is available for highly dynamic applications under a fast oscillation, while the phantom soft hand is inadequate because its compliant fingers are susceptible to unfavorable deformation due to large acceleration. The third soft robot prototype is a snake robot made by connecting multiple OASS actuators traveled by the waves generated by the bending of the actuators (using the soft side) and crossing a gap larger than 75% of its body length owing to the high stiffness of the rigid side.

Supporting Information

Supporting Information is available from the Wiley Online Library or from the author.

Acknowledgements

The authors acknowledge the support of the following: in part by the National Key R&D Program of China under (grant no.: 2022YFB4701200), in part by the National Natural Science Foundation of China under (grant no.: 52275021), in part by the Science, Technology, and Innovation Commission of Shenzhen Municipality under (grant no.: ZDSYS20200811143601004), and in part by Southern Marine Science and Engineering Guangdong Laboratory (Guangzhou) under (grant no.: K19313901).

Conflict of Interest

The authors declare no conflict of interest.

Data Availability Statement

The data that support the findings of this study are available in the supplementary material of this article.

Keywords

anisotropic stiffness, bioinspired, origami, soft robots

Received: September 8, 2022

Revised: January 24, 2023

Published online:

- [1] D. Trivedi, C. D. Rahn, W. M. Kier, I. D. Walker, *Appl. Bionics Biomech.* **2008**, *5*, 99.
- [2] Z. Song, Z. Fu, D. Romano, P. Dario, J. S. Dai, *Soft Rob.* **2022**, *9*, 440.
- [3] P. Polygerinos, N. Correll, S. A. Morin, B. Mosadegh, C. D. Onal, K. Petersen, M. Cianchetti, M. T. Tolley, R. F. Shepherd, *Adv. Eng. Mater.* **2017**, *19*, 1700016.
- [4] T. Arnold, M. Scheutz, *Soft Rob.* **2017**, *4*, 81.
- [5] J. Shintake, V. Cacucciolo, D. Floreano, H. Shea, *Adv. Mater.* **2018**, *30*, 1707035.
- [6] S. Yang, Y. Zhou, I. D. Walker, C. Yang, D. T. Branson, Z. Song, J. S. Dai, R. Kang, *IEEE/ASME Trans. Mechatron.* **2022**, <https://doi.org/10.1109/TMECH.2022.3219108>.
- [7] Y. Wei, Y. H. Chen, T. Ren, Q. Chen, C. X. Yan, Y. Yang, Y. T. Li, *Soft Rob.* **2016**, *3*, 134.
- [8] Y. Yang, Y. Chen, Y. Li, Z. Wang, Y. Li, *Soft Rob.* **2017**, *4*, 338.
- [9] Y. S. Narang, J. J. Vlassak, R. D. Howe, *Adv. Funct. Mater.* **2018**, *28*, 1707136.
- [10] D. S. Shah, J. P. Powers, L. G. Tilton, S. Kriegman, J. Bongard, R. Kramer-Bottiglio, *Nat. Mach. Intell.* **2021**, *3*, 51.
- [11] D. Y. Lee, S. R. Kim, J. S. Kim, J. J. Park, K. J. Cho, *Soft Rob.* **2017**, *4*, 163.
- [12] A. Yin, H. C. Lin, J. Thelen, B. Mahner, T. Ranzani, *Adv. Intell. Syst.* **2019**, *1*, 1900089.
- [13] X. Dong, C. Tang, S. Jiang, Q. Shao, H. Zhao, *IEEE Rob. Autom. Lett.* **2021**, *6*, 2405.
- [14] T. Liu, H. Xia, D. Y. Lee, A. Firouzeh, Y. L. Park, K. J. Cho, *IEEE Rob. Autom. Lett.* **2021**, *6*, 8078.
- [15] J. Shintake, B. Schubert, S. Rosset, H. Shea, D. Floreano, in *IEEE/RSJ Int. Conf. on Intelligent Robots and Systems (IROS)*, IEEE, Hamburg, Germany, September–October **2015**.
- [16] J. Kim, W. Y. Choi, S. Kang, C. Kim, K. J. Cho, *IEEE Trans. Robot.* **2019**, *35*, 1475.
- [17] M. E. Giannaccini, C. Xiang, A. Atyabi, T. Theodoridis, S. Nefti-Meziani, S. Davis, *Soft Rob.* **2018**, *5*, 54.
- [18] B. Zhang, W. Zhang, Z. Zhang, Y. F. Zhang, H. Hingorani, Z. Liu, J. Liu, Q. Ge, *ACS Appl. Mater. Interfaces* **2019**, *11*, 10328.
- [19] B. Zhang, H. Li, J. Cheng, H. Ye, A. H. Sakhaei, C. Yuan, P. Rao, Y. F. Zhang, Z. Chen, R. Wang, X. He, J. Liu, R. Xiao, S. Qu, Q. Ge, *Adv. Mater.* **2021**, *33*, e2101298.
- [20] Y. Zhang, N. Zhang, H. Hingorani, N. Ding, D. Wang, C. Yuan, B. Zhang, G. Gu, Q. Ge, *Adv. Funct. Mater.* **2019**, *29*, 1806698.
- [21] S. Shian, K. Bertoldi, D. R. Clarke, *Adv. Mater.* **2015**, *27*, 6814.
- [22] T. Li, Z. Zou, G. Mao, X. Yang, Y. Liang, C. Li, S. Qu, Z. Suo, W. Yang, *Soft Rob.* **2019**, *6*, 133.
- [23] S. Sun, J. Yang, W. Li, H. Deng, H. Du, G. Alici, *Smart Mater. Struct.* **2015**, *24*, 085021.
- [24] S. Muraio, K. Hirata, F. Miyasaka, *IEEE Trans. Magn.* **2015**, *52*, 1.

- [25] S. Baeckens, D. K. Wainwright, J. C. Weaver, D. J. Irschick, J. B. Losos, *J. Anat.* **2019**, 235, 346.
- [26] C. Broeckhoven, G. Diedericks, P. L. N. Mouton, *J. Anim. Ecol.* **2015**, 84, 1213.
- [27] C. Chang, P. Wu, R. E. Baker, P. K. Maini, L. Alibardi, C. M. Chuong, *Int. J. Dev. Biol.* **2009**, 53, 813.
- [28] A. M. Peattie, C. Majidi, A. Corder, R. J. Full, *J. R. Soc. Interface* **2007**, 4, 1071.
- [29] L. Alibardi, L. Dalla Valle, A. Nardi, M. Toni, *J. Anat.* **2009**, 214, 560.
- [30] C. S. Rutland, P. Cigler, V. Kubale, *Veterinary Anatomy and Physiology*, IntechOpen, London, UK **2019**.
- [31] R. H. Sawyer, T. Glenn, J. O. French, B. Mays, R. B. Shames, G. L. Barnes Jr, W. Rhodes, Y. Ishikawa, *Am. Zool.* **2000**, 40, 530.
- [32] M. Somireddy, A. Czekanski, *Mater. Des.* **2020**, 195, 108953.
- [33] H. Zhang, K. F. Wu, G. M. Xiao, Y. X. Du, G. H. Tang, *Compos. Struct.* **2021**, 267, 113870.
- [34] J. Chen, X. Liu, Y. Tian, W. Zhu, C. Yan, Y. Shi, L. B. Kong, H. J. Qi, K. Zhou, *Adv. Mater.* **2022**, 34, 2102877.
- [35] T. Ding, J. Z. Xiao, S. Zou, X. J. Zhou, *Compos. Struct.* **2020**, 254, 112808.
- [36] R. V. Martinez, C. R. Fish, X. Chen, G. M. Whitesides, *Adv. Funct. Mater.* **2012**, 22, 1376.
- [37] R. V. Martinez, J. L. Branch, C. R. Fish, L. Jin, R. F. Shepherd, R. M. Nunes, Z. Suo, G. M. Whitesides, *Adv. Mater.* **2013**, 25, 205.
- [38] Z. Chen, B. Tighe, J. G. Zhao, *IEEE/ASME Trans. Mechatron.* **2022**, 27, 2016.
- [39] J. Huang, J. Zhou, Z. Wang, J. Law, H. Cao, Y. Li, H. Wang, Y. Liu, *Adv. Intell. Syst.* **2022**, 4, 2200081.
- [40] M. Salerno, K. Zhang, A. Menciassi, J. S. Dai, *IEEE Trans. Rob.* **2016**, 32, 484.
- [41] S. Miyashita, S. Guitron, S. Li, D. Rus, *Sci. Rob.* **2017**, 2, aao4369.
- [42] S. Miyashita, S. Guitron, K. Yoshida, S. Li, D. D. Damian, D. Rus, *2016 Int. Conf. on Robotics and Automation (ICRA)*, IEEE, Stockholm, Sweden, May **2016**.
- [43] Y. Lin, G. Yang, Y. Liang, C. Zhang, W. Wang, D. Qian, H. Yang, J. Zou, *Adv. Funct. Mater.* **2020**, 30, 2000349.
- [44] B. H. Chen, Z. Y. Shao, Z. X. Xie, J. Q. Liu, F. Pan, L. W. He, L. Zhang, Y. M. Zhang, X. C. Ling, F. J. Peng, W. D. Yun, L. Wen, *Adv. Intell. Syst.* **2021**, 3, 2000251.
- [45] W. Kim, J. Eom, K.-J. Cho, *Adv. Intell. Syst.* **2022**, 4, 2100176.
- [46] S. G. Li, J. J. Stampfli, H. J. Xu, E. Malkin, E. V. Diaz, D. Rus, R. J. Wood, in *2019 Int. Conf. on Robotics and Automation (ICRA)*, IEEE, Montreal, Canada, May **2019**.
- [47] C. D. Onal, R. J. Wood, D. Rus, *IEEE/ASME Trans. Mechatron.* **2012**, 18, 430.
- [48] C. H. Belke, J. Paik, *IEEE/ASME Trans. Mechatron.* **2017**, 22, 2153.
- [49] C. Lv, D. Krishnaraju, G. Konjevod, H. Yu, H. Jiang, *Sci. Rep.* **2014**, 4, 5979.
- [50] C. Ai, Y. Chen, L. Xu, H. Li, C. Liu, F. Shang, Q. Xia, S. Zhang, *Adv. Eng. Mater.* **2021**, 23, 2100473.
- [51] E. T. Filipov, T. Tachi, G. H. Paulino, *P. Natl. Acad. Sci. U.S.A* **2015**, 112, 12321.
- [52] H. Y. Zhu, Z. X. Li, R. K. Wang, S. Y. Chen, C. L. Zhang, F. Y. Li, *Materials* **2021**, 14, 6374.
- [53] T. Tachi, K. Miura, *J. Int. Assoc. Shell Spatial Struct.* **2012**, 53, 217.
- [54] E. T. Filipov, K. Liu, T. Tachi, M. Schenk, G. H. Paulino, *Int. J. Solids Struct.* **2017**, 124, 26.
- [55] H. Fang, S. A. Chu, Y. Xia, K. W. Wang, *Adv. Mater.* **2018**, 30, 1706311.
- [56] K. C. Cheung, T. Tachi, S. Calisch, K. Miura, *Smart Mater. Struct.* **2014**, 23, 094012.
- [57] Z. W. Lin, L. S. Novelino, H. M. Wei, N. A. Alderete, G. H. Paulino, H. D. Espinosa, S. Krishnaswamy, *Small* **2020**, 16, 2002229.
- [58] L. Mahadevan, S. Rica, *Science* **2005**, 307, 1740.
- [59] S. A. Zirbel, R. J. Lang, M. W. Thomson, D. A. Sigel, P. E. Walkemeyer, B. P. Trease, S. P. Magleby, L. L. Howell, *J. Mech. Des.* **2013**, 135.
- [60] D. R. Ellis, M. P. Venter, G. Venter, *Soft Rob.* **2021**, 8, 478.
- [61] Z. Wang, K. Li, Q. He, S. Cai, *Adv. Mater.* **2019**, 31, 1806849.
- [62] W. Hu, G. Z. Lum, M. Mastrangeli, M. Sitti, *Nature* **2018**, 554, 81.
- [63] S. A. Morin, R. F. Shepherd, S. W. Kwok, A. A. Stokes, A. Nemiroski, G. M. Whitesides, *Science* **2012**, 337, 828.
- [64] M. T. Tolley, R. F. Shepherd, B. Mosadegh, K. C. Galloway, M. Wehner, M. Karpelson, R. J. Wood, G. M. Whitesides, *Soft Rob.* **2014**, 1, 213.
- [65] L. Qin, X. Liang, H. Huang, C. K. Chui, R. C. Yeow, J. Zhu, *Soft Rob.* **2019**, 6, 455.
- [66] I. Must, F. Kaasik, I. Poldsalu, L. Mihkels, U. Johanson, A. Punning, A. Aabloo, *Adv. Eng. Mater.* **2015**, 17, 84.
- [67] C. Sung, D. Rus, *Robotics Research*, Springer, Cham, Switzerland **2018**, Ch. 16.
- [68] J. W. Cao, L. Qin, J. Liu, Q. Y. Ren, C. C. Foo, H. Q. Wang, H. P. Lee, J. Zhu, *Extreme Mech. Lett.* **2018**, 21, 9.
- [69] Z. Jiao, C. Ji, J. Zou, H. Yang, M. Pan, *Adv. Mater. Technol.* **2019**, 4, 1800429.
- [70] M. Raibert, K. Blankespoor, G. Nelson, R. Playter, *IFAC Proc. Vol.* **2008**, 41, 10822.
- [71] S. A. Dalley, T. E. Wiste, T. J. Withrow, M. Goldfarb, *IEEE/ASME Trans. Mechatron.* **2009**, 14, 699.
- [72] R. Deimel, O. Brock, *Int. J. Rob. Res.* **2016**, 35, 161.
- [73] H. Zhao, K. O'Brien, S. Li, R. F. Shepherd, *Sci. Rob.* **2016**, 1, aai7529.
- [74] S. D. Han, S. W. Feng, J. Yu, *IEEE Rob. Autom. Lett.* **2019**, 5, 446.
- [75] F. Bourbonnais, P. Bigras, I. A. Bonev, *IEEE/ASME Trans. Mechatron.* **2014**, 20, 740.
- [76] Q. Xiong, B. W. K. Ang, T. Jin, J. W. Ambrose, R. C. H. Yeow, *Adv. Intell. Syst.* **2022**, 2200346.
- [77] R. Kang, Y. Guo, L. Chen, D. T. Branson, J. S. Dai, *IEEE/ASME Trans. Mechatron.* **2016**, 22, 751.
- [78] C. Yang, S. Geng, I. Walker, D. T. Branson, J. Liu, J. S. Dai, R. Kang, *Int. J. Rob. Res.* **2020**, 39, 1620.